

3-D SAR Imaging Based RCS Measurement Technique with Fixed Transmitter

Ke-Fei Liao*, Xiao-Ling Zhang, and Jun Shi

Abstract—To avoid the spatial variation of scattering characteristic effect, a three-dimensional synthetic aperture radar (3-D SAR) imaging based radar cross section (RCS) extraction technique with fixed transmitter is developed. The 3-D SAR image is used to extract targets' RCS, so it can spatially distinguish different parts of a complex object, or the targets' RCS from environment. With the abilities of outdoor measurement, it can greatly reduce the cost of measurement. Two simulations of three squares and a 3-D complex-shaped electric-large flight model demonstrate the accurate prediction of RCS.

1. INTRODUCTION

Radar target characterization is of great importance in both military and civilian applications, e.g., rescue mission for searching survivors in earthquake and orbiting object identification. The direct determination of the far-field radar cross section (RCS) typically requires not only expensive anechoic chambers to reduce the environment noise [1–3], but also expensive long range measurement arrangements or compact range measuring equipment [4]. To overcome these defects, many imaging based RCS measurement techniques are developed. The most practical and mature ones are based on synthetic aperture radar (SAR) imaging to model the target's scattering, such as inverse SAR imaging based RCS measurement [5–8] and linear array SAR imaging based RCS measurement [9–11].

According to the results in [10], for synthetic aperture technique, the spatial variation of scattering characteristic will cause acquired data non-coherent and deteriorate the SAR image quality greatly when the aperture angle is rather large. To eliminate the variation, the transmitter needs to be fixed. Since the transmitted signal and the geometry of the transmitter and targets remain unchanged during the observation session, the coherence of scattering electric field is well preserved, which is crucial for SAR imaging.

Based on these, the RCS extraction technique based on 3-D SAR imaging with fixed transmitter is developed, which can eliminate the spatial variation of scattering characteristic so as to improve the RCS measurement precision. The basic idea of the technique is transforming the near-field electric/magnetic currents that the 3-D SAR imaging technique reconstructed to far-field, and using the FFT algorithm to recover the frequency response of RCS. Thus, the backscattering monostatic RCS and non-backscattering bistatic RCS can be obtained as a function of direction and frequency. In addition, by rotating the target, the non-backscattering monostatic RCS can also be obtained.

Owing to its advantages such as 3-D high resolution capability, the technique can spatially distinguish the RCS of different parts from a complex object, or the targets' RCS from environment, which is available for outdoor measurement.

To generate the scattering fields of simulation targets, the widely accepted software FEKO based on physical optics is employed. The RCS results of simulation targets are compared to the FEKO results to verify the ROI extraction and precision of the technique.

Received 3 January 2015, Accepted 20 March 2015, Scheduled 5 April 2015

* Corresponding author: Ke-Fei Liao (kefeiliao@gmail.com).

The authors are with the Electronic Engineering Department, University of Electronic Science and Technology of China, No. 2006, Xiyuan Road, Chengdu, Sichuan 611731, China.

2. PRINCIPLE

In this section the scattering explanation of 3-D SAR image will be introduced. Then, by using 3-D SAR image, the RCS extraction technique will be presented.

2.1. Scattering Explanation of 3-D SAR Image

When the transmitter is fixed, since the transmitted signal and geometry of the transmitter and targets remain unchanged during the observation session, the coherence of scattering electric field is well preserved. Then, the mechanism of 3-D SAR imaging can be explained using the scattering theory [12–14], which separates the scattering phenomenon into three stages:

Firstly, the incident electromagnetic wave inspires the induced electric/ magnetic currents on the targets (see Fig. 1);

Secondly, the induced electric/magnetic currents produce the receiver array propagating in free space (see Fig. 2);

Thirdly, 3-D imaging methods (such as back-projection (BP) algorithm) are employed to obtain 3-D image.

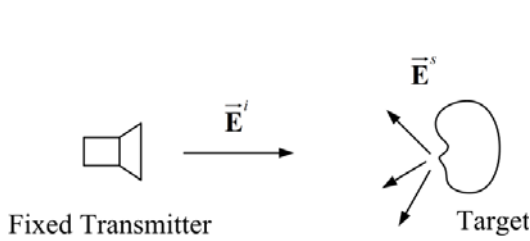


Figure 1. Geometry of transmitter and target, since the transmitted wave and the geometry remain unchanged during the observation session, the induced electric/ magnetic current is always same. For RCS measurement, the transmitter should be placed far away enough from target to meet the far-field requirement.

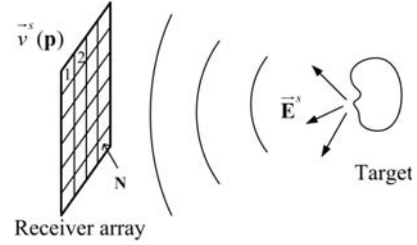


Figure 2. Geometry of (virtual) receiver array and scattering field, the receiver acquires the scattering field over a large spatial scale, and then 3-D image can be obtained by using 3-D imaging methods.

Note that, for RCS measurement, the far-field incident electromagnetic wave is required in stage one. To meet the requirement, the transmitter should be placed far enough from target, or the near-field to far-field transformation of incident field should be employed which will be studied in the future.

In stage two, denoting the polarization direction of the receiver antenna as $\hat{\mathbf{a}}$ and the position of receiver in the receiver array as \mathbf{p} , the received voltage at \mathbf{p} is the scattering of the induced electric/magnetic currents projected to $\hat{\mathbf{a}}$, which can be expressed as [10]:

$$v(\mathbf{p}, \omega) = \int_{V'} j\hat{\mathbf{a}} \cdot [\omega\mu\mathbf{J} - K(\mathbf{M} \times \hat{\mathbf{p}})] \psi d\mathbf{p}' \quad (1)$$

where, ω denotes the temporal frequency, μ the permeability, \mathbf{J} the volume electric current density, \mathbf{M} the volume magnetic current density, $\hat{\mathbf{p}} = (\mathbf{p}' - \mathbf{p})/|\mathbf{p}' - \mathbf{p}|$ the directional vectors from the target at \mathbf{p}' to the receiver at \mathbf{p} , K denotes the wave number, and $K = \omega/c$, ψ the green function:

$$\psi = \frac{e^{jK|\mathbf{p}' - \mathbf{p}|}}{4\pi|\mathbf{p}' - \mathbf{p}|} \quad (2)$$

In stage three, the 3-D SAR employs 3-D imaging methods to reconstruct the 3-D image of the targets. According to [10], the (complex) values of the 3-D image is estimation $\vec{\mathbf{X}}_a(\mathbf{p}')$ of the superposition of the $\vec{\mathbf{J}}$ and the outer product of $\vec{\mathbf{M}}$ and the unit vector from the virtual array

center to the pixel $\hat{\mathbf{p}}'$, $\hat{\mathbf{p}}'$ indicates the directional vectors from the receiver \mathbf{p} to the target at \mathbf{p}' , $\hat{\mathbf{p}}' = (\mathbf{p} - \mathbf{p}')/|\mathbf{p} - \mathbf{p}'|$:

$$\bar{\mathbf{X}}_a(\mathbf{p}') \approx \mu \hat{\mathbf{a}} \mathbf{J}(\mathbf{p}') - c^{-1} \hat{\mathbf{a}} \cdot [\mathbf{M}(\mathbf{p}') \times \eta \hat{\mathbf{p}}'] \quad (3)$$

where, η represents the system deviation of 3-D imaging system caused by the magnetic current density, when the aperture angle is smaller than 20 degree, $\eta > 0.98$, which can be ignored in practice [10].

For perfect conductor, the (complex) values of the 3-D image is only estimation $\bar{\mathbf{J}}_a(\mathbf{p}')$ of the $\vec{\mathbf{J}}$:

$$\bar{\mathbf{J}}_a(\mathbf{p}') \approx \mu \hat{\mathbf{a}} \mathbf{J}(\mathbf{p}') \quad (4)$$

With Eqs. (3) and (4), we have 3-D distribution of the induced electric and magnetic currents. In this paper, we will use this 3-D distribution to extract and calculate the targets' RCS.

2.2. Selective Feature Extraction

Since 3-D SAR imaging technique can completely separate the electric/magnetic current of different parts of target and ambient interference (such as ground, wall and turntable, etc.) spatially, RCS measurement using 3-D SAR image can relax the requirement to the measurement environment, or extract the RCS of different parts of target. The selective feature extraction (SFE) from 3-D SAR image needs two steps.

The first step of SFE is to use the prior-information (locations and sizes of targets) to extract the region of interested (ROI), i.e., the region that includes the targets and excludes the environmental disturbance, or the interested parts of the targets.

The second step is to remove the side-lobe deflection caused by $\chi_{\mathbf{J}}(\mathbf{p}'', \mathbf{p}')$. To do this, a binary image should be generated to separate the main-lobes and the side-lobes without changing the complex pixel values in the ROI of SAR image as

$$\Omega(\mathbf{p}') = \begin{cases} 1 & |\bar{\mathbf{J}}_a(\mathbf{p}')| \text{ or } |\bar{\mathbf{X}}_a(\mathbf{p}')| \geq \xi \\ 0 & |\bar{\mathbf{J}}_a(\mathbf{p}')| \text{ or } |\bar{\mathbf{X}}_a(\mathbf{p}')| < \xi \end{cases} \quad \mathbf{p}' \in \text{ROI} \quad (5)$$

where the minimum desirable pixel value on the sharpened image, ξ , should be selected small enough not to miss any $\vec{\mathbf{J}}$ and $\vec{\mathbf{M}}$. The unnecessary side-lobes can be removed by element-wise multiplication of the $\Omega(\mathbf{p}')$ with the ROI of SAR image

$$\bar{\mathbf{J}}'_a(\mathbf{p}') = \Omega(\mathbf{p}') \cdot \bar{\mathbf{J}}_a(\mathbf{p}'), \text{ or } \bar{\mathbf{X}}'_a(\mathbf{p}') = \Omega(\mathbf{p}') \cdot \bar{\mathbf{X}}_a(\mathbf{p}') \quad (6)$$

to obtain a sharpened image in the ROI.

2.3. Far-Field RCS Extraction

As we stated in subsection 2.1, for perfect conductor, 3-D SAR image reflects the accurate electric current density. After SFE, we can reconstruct the scattering field (reconstructed voltage exactly) by using (1). But according to the geometry of 3-D SAR, the kernel ψ used in (1) is a near-field kernel. To obtain far-field RCS, this could be remedied by using a far field kernel when $|\mathbf{p}| \rightarrow \infty$ as:

$$\psi_{far} = \frac{e^{jK|\mathbf{p}|} e^{jK\hat{\mathbf{p}} \cdot \mathbf{p}'}}{4\pi |\mathbf{p}|} \quad (7)$$

Thus, the far-field voltage can be reconstructed as:

$$v_{far}(\hat{\mathbf{p}}, t) = \int_{ROI} j\omega \bar{\mathbf{J}}'_a(\mathbf{p}') \psi_{far} d\mathbf{p}' \quad (8)$$

where, $\hat{\mathbf{p}}$ denotes the directional vectors from the target at \mathbf{p}' to the receiver at \mathbf{p} .

As $v_{far}(\hat{\mathbf{p}}, t)$ is the superposition of wideband components from the wideband SAR system, to obtain the frequency response of $v_{far}(\hat{\mathbf{p}}, t)$, the FFT operator is used, and we have:

$$v_{far}(\hat{\mathbf{p}}, \omega) = FFT[v_{far}(\hat{\mathbf{p}}, t)] \quad (9)$$

Then, the RCS can be calculated as:

$$\sigma_{far}(\hat{\mathbf{p}}, \omega) = 16\pi^2 |\mathbf{p}|^2 |\mathbf{p}_{in}|^2 \left(\frac{v_{far}(\hat{\mathbf{p}}, \omega)}{v_{in}(\omega)} \right)^2 \quad (10)$$

where, $v_{in}(\omega)$ denotes the voltage of transmitter placed at \mathbf{p}_{in} (assumed that the transmitter is placed far away enough from target to meet the far-field requirement).

Equation (10) indicates that using 3-D SAR image via BP method, we can obtain far-field RCS of perfect conductor as a function of frequency and direction in some configurations. The direction angles can be calculated and are limited as:

$$|\Theta| \leq \arctan \frac{L}{2R} \quad (11)$$

where, L means the length of receiver array and R the distance between the targets and the center of the array.

As the transmitter is fixed and the receiver can be seen as moves in the array, when the receiver is at the same direction angles as the transmitter, the monostatic RCS can be obtain as a function of direction and frequency; when the receiver is not at the same direction angles as the transmitter, the bistatic RCS is obtained as a function of direction and frequency, and the bistatic angles which can be calculated are limited as Eq. (11). In this case, only the monostatic RCS in one angle and the bistatic RCS in different angles within a certain range are obtained. If monostatic RCS of different angles is needed, one should rotate the target at different angles. Moreover, by rotating the target, the range of angles of the bistatic RCS can also be extended.

Strictly speaking, to predict RCS of general dielectric medium, we need to know both of the electric/magnetic currents. Since the BP method can only obtain the superposition of \mathbf{J} and $\mathbf{M} \times \hat{\mathbf{p}}$, we cannot calculate the voltage accurately.

When $\mathbf{p} = 0$, however, $\hat{\mathbf{p}} = \frac{\mathbf{p}'}{|\mathbf{p}'|} = \hat{\mathbf{p}}'$, ignoring the system derivation η , and we have:

$$v(0, t) = \int_{ROI} j\hat{\mathbf{a}} \cdot [\mu\mathbf{J} - c^{-1}(\mathbf{M} \times \hat{\mathbf{p}}')] \psi d\mathbf{p}' \approx \int_{ROI} \bar{\mathbf{X}}_a(\mathbf{p}') \psi d\mathbf{p}' \quad (12)$$

which is in accordance with the imaging result of BP method.

Equation (12) indicates that using the 3-D SAR image via BP method, we can restore the voltage at the original point with slight system derivation and predict backscattering RCS of general dielectric medium properly. When predicting the non-backscattering RCS, however, additional error occurs because of the unknown electric/magnetic current densities.

3. SIMULATION EXPERIMENT

In this section, the well-accepted electromagnetic calculation software FEKO based on physical optics [15] is used to simulate the scattered fields and set the theoretical RCS of targets. Two Experiments are conducted to verify ROI extraction and precision of the technique by comparing with FEKO results.

3.1. RCS of ROI Extraction

The technique has been applied to a three-dimensional target distribution made up of three perfect-conductor thin square plates with lengths of 2, 2.5 and 3 cm, respectively, and positioned as shown in Table 1 and Fig. 3. The center frequency is 2 GHz, the bandwidth 1 GHz, and the size of receiver array 2 m \times 2 m.

Figure 4 shows the 3-D imaging result of the three thin square plates, and each of them can be easily extracted from the whole image by using the prior-information (locations and sizes). Then, the RCS of each plate can be independently calculated by using the technique stated in this paper, and these are shown in Figs. 5–6.

Very good correspondence between FEKO and simulation is observed in Fig. 5. Small deviations are seen in Fig. 6 at the band edges due to the finite-length filter used in the range domain. Other

Table 1. The squares positional information.

Point	Model	Location		
		$X(m)$	$Y(m)$	$Z(m)$
A	2 cm plate	0.00	0.00	1.85
B	2.5 cm plate	0.30	0.30	1.70
C	3 cm plate	-0.30	-0.30	2.00

Table 2. Deviation of RCS of squares (dB).

Point	RCS of Fig. 5		RCS of Fig. 6	
	Mean difference	Standard deviation	Mean difference	Standard deviation
A	0.107	0.042	0.350	0.320
B	0.083	0.043	0.345	0.316
C	0.083	0.048	0.337	0.309
Total	0.524	0.485	0.480	0.398

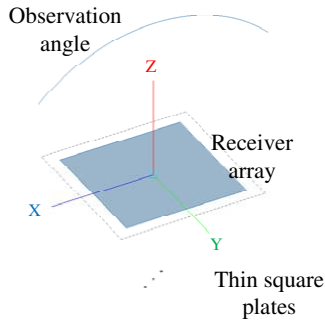


Figure 3. Geometry of three thin square plates, the observation angle is from -45° to 45° .

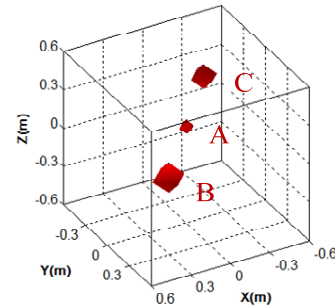


Figure 4. 3-D imaging result of three thin square plates and each one of them can be easily extracted by using the prior-information (locations and sizes).

very small differences (See Table 2) are probably due to the finite-length interpolations used in the BP algorithm and RCS calculation.

3.2. Complicated Flight Mode

The scattering characteristic of flight model is complicated, and the spatial variation of scattering characteristic from different observation angle is significant, which is suitable for verifying the prediction of RCS measurement. Fig. 7 shows geometry of the flight model, in which the center frequency is 10 GHz, the bandwidth 5 GHz, and the size of receiver array $2\text{ m} \times 2\text{ m}$.

Figure 9 shows the angle responses of RCS. When observation angle is between -20 and 20 degrees, very good correspondence between FEKO and simulation is observed, and the mean difference is 2.843 dB and the standard deviation 1.033 dB. When observation angle is less than -20 degrees or more than 20 degrees, deviations are noticeable due to the system deviation stated in (8). This disadvantage can be solved by rotating the target to obtain the angle responses of RCS more than 20 degree.

Figure 10 shows the frequency responses of RCS. The variation trends of two results are approximately the same, but the mean difference is 2.719 dB. The standard deviation is 1.941 dB due to the finite-length interpolations and some loss of small scattering characteristic suffered from the discrete

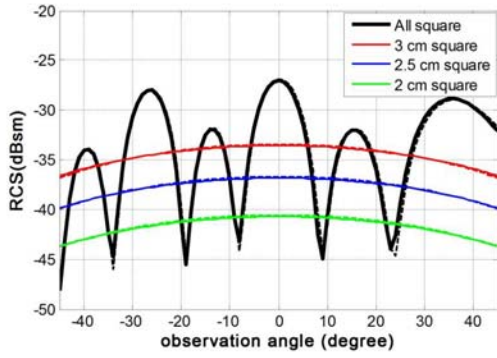


Figure 5. RCS of all thin square plates and individual scattering from different observation angles at the center frequency 2 GHz (dashed lines show the FEKO results).

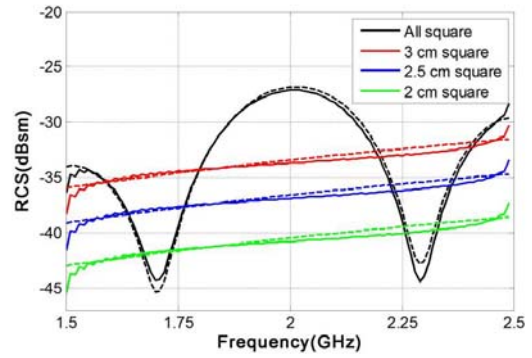


Figure 6. RCS of all thin square plates and individual scattering from different frequencies at the observation angle 0° (dashed lines show the FEKO results).

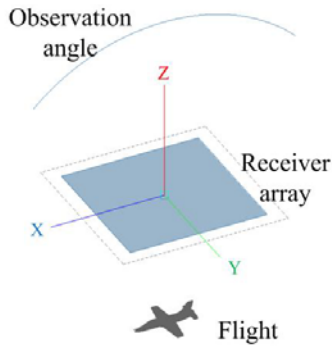


Figure 7. Geometry of flight model, the observation angle is from -45° to 45° .

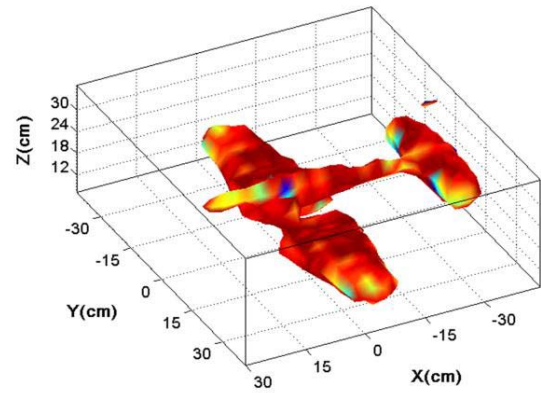


Figure 8. 3-D imaging result of the flight model.

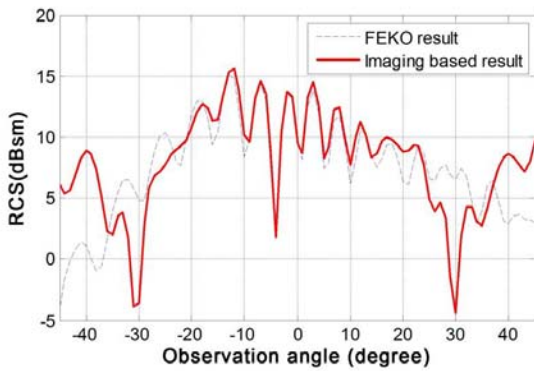


Figure 9. RCS of the flight model from different observation angles at the center frequency 10 GHz.

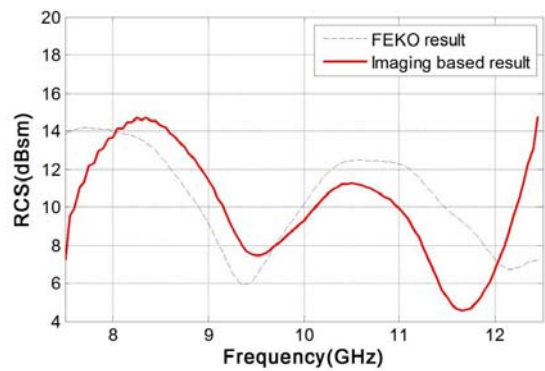


Figure 10. RCS of the flight model from different frequencies at 0° .

3-D resolution equal to the wavelength. By contrast, the electromagnetic computing requires the mesh size of target to be less than one-eighth of the wavelength, which cannot be satisfied in all the imaging based RCS prediction techniques.

According to the above reason, the precisions of measuring complicated targets are limited due to the system resolution. However, considering that the 2-D/3-D radar imaging techniques have been used more and more [16, 17], the imaging based RCS measurement results are more practical and useful than the electromagnetic computing results.

4. CONCLUSION

A novel 3-D SAR imaging based RCS measurement technique with fixed transmitter has been presented, which can avoid the spatial variation of scattering characteristic effect so as to improve the RCS measurement precision. With the abilities of selective feature extraction, it can relax the requirement to the measurement environment and reduce the cost of measurement. Meanwhile, the individual and integral RCSes of targets can be obtained as to analyze the RCS of interested parts. This process has been demonstrated by 3-D simulation and shown to provide high-accuracy results. The technique is more practical and useful since 2-D/3-D radar imaging techniques has been used more and more nowadays.

ACKNOWLEDGMENT

This work was supported by the National Natural Science Foundation of China under Grant [No. 61101170]; Outstanding Ph.D. Foundation of the University of Electronic Science and Technology of China (UESTC) under Grant [No. A1098524023901001008].

REFERENCES

1. Sheen, D., D. McMakin, and T. Hall, "Near-field three-dimensional radar imaging techniques and applications," *Applied Optics*, Vol. 49, No. 19, E83–E93, 2010.
2. Cown, B. J. and C. Ryan, Jr., "Near-field scattering measurements for determining complex target RCS," *IEEE Trans. Anten. Propag.*, Vol. 31, No. 5, 576–595, 1989.
3. Hu, C. F., J. D. Xu, N. J. Li, et al., "Indoor accurate RCS measurement technique on UHF band," *Progress In Electromagnetics Research*, Vol. 81, 279–289, 2008.
4. Broquetaset, A., et al., "A compact system for radar cross section measurement and imaging up to 40 GHz," *Proc. JINA*, 596–599, Nice, France, 1990.
5. Antoni, B., P. Josep, L. Jofre, and C. Angel, "Spherical wave near-field imaging and radar cross-section measurement," *IEEE Trans. Anten. Propag.*, Vol. 46, No. 5, 730–735, 1998.
6. Nicholson, K. J. and C. H. Wang, "Improved near-field radar cross-section measurement technique," *IEEE Anten. Wirel. Propag. Letters*, Vol. 8, 1103–1106, 2009.
7. Thomas, V. and F. E. Thomas, "Comparison and application of near-field isar imaging techniques for far-field radar cross section determination," *IEEE Trans. Anten. Propag.*, Vol. 54, No. 1, 144–151, 2006.
8. Li, S., B. Zhu, and H. Sun, "NUFFT-based near-field imaging technique for far-field radar cross section calculation," *IEEE Anten. Wirel. Propag. Letters.*, Vol. 9, 550–553, 2010.
9. Woo, J. C., B. G. Lim, S. M. Lee, et al., "Near-field-to-far-field transformation using wavenumber migration technique for a 3D spotlight SAR," *3rd APSAR*, Seoul, Korea, 2011.
10. Shi, J., K. F. Liao, and X. L. Zhang, "Three-dimensional SAR with fixed transmitter and its scattering explanation," *Progress In Electromagnetics Research*, Vol. 133, 285–307, 2013.
11. Ford, K. L., J. C. Bennett, and D. G. Holtby, "Use of a plane-wave synthesis technique to obtain target RCS from near-field measurements, with selective feature extraction capability," *IEEE Trans. anten. propag.*, Vol. 61, No. 4, 2051–2057, 2013.

12. Knott, E. F., J. F. Shaeffer, and M. T. Tuley, *Radar Cross Section, Its Prediction, Measurement and Reduction*, Artech House, Inc., 1985.
13. Knott, E. F., J. F. Shaeffer, and M. T. Tuley, *Radar Cross Section*, 2nd Edition, Artech House, Inc., 1993.
14. Sheppard, Jr., C., A. Choudhury, and J. Gannaway, "Electromagnetic field near the focus of wide-angular lens and mirror systems," *IEE J. Microw. Optics Acous.*, Vol. 1, No. 4, 129-132, 1977.
15. Smit, J. C., J. E. Cilliers, and E. H. Burger, "Comparison of MLFMM, PO and SBR for RCS investigations in radar applications," *IET Intern. Conf. Radar Sys.*, Glasgow UK, 2012.
16. Yan, W., et al., "A novel 3-D imaging technique for interferometric circular SAR system," *IEEE URSI GASS*, 2014.
17. Wei, S. J., X. L. Zhang, J. Shi, et al., "Sparse array microwave 3-D imaging: Compressed sensing recovery and experimental study," *Progress In Electromagnetics Research*, Vol. 135, 161–181, 2013.